PCCP

Accepted Manuscript

ROYAL SOCIETY
OF **CHEMISTRY**

www.rsc.org/pccp

ARTICLE TYPE www. rsc.org/x XXXXXXXX

Energy flow between spectral components in 2D Broadband Stimulated Raman Spectroscopy

G. Batignani[a,b], **G. Fumero**[a], **S. Mukamel**[c] **and T. Scopigno**[a,d*]

a Dipartimento di Fisica, Universitá di Roma “Sapienza”, I-00185 Roma (Italy).
b Dipartimento di Scienze Fisiche e Chimiche, Universitá degli Studi dell’Aquila , I-67100, L’Aquila (Italy).
c Department of Chemistry, University of California, Irvine, California 92697-2025 (USA).
d Centre for Life Nano Science – IIT@Sapienza, Istituto Italiano di Tecnologia, I-00161 Roma (Italy).

Received Xth XXXXXXXXXX 20XX, Accepted Xth XXXXXXXXX 20XX
First published on the web Xth XXXXXXXXXX 200X

DOI: 10.1039/b000000x

We introduce a general theoretical description of non resonant impulsive Femtosecond Stimulated Raman Spectroscopy in a multimode harmonic model. In this technique an ultrashort actinic pulse creates coherences of low frequency modes and is followed by a pair of a narrowband Raman and broadband probe pulse. Using Closed-Time-Path-Loop (CTPL) diagrams, the response on both the red and the blue sides of the broadband pulse with respect to the narrowband Raman pulse is calculated, the process couples high and low frequency modes which share the same ground state. The transmitted intensity oscillates between the red and the blue side, while the total number of photons is conserved. The total energy of the probe signal is periodically modulated in time by the coherence created in the low frequency modes.

1 Introduction

Nonlinear optical techniques have been widely employed in time resolved studies of vibrational dynamics of complex molecular and solid state systems.

Stimulated Raman Scattering (SRS) is a nonlinear third order four-wave mixing process, which is coherently driven when the energy difference between two laser pulses is resonant with a Raman active molecular transition. Scattering from the interacting medium generates blue and red shifted components with an efficiency which is enhanced by many orders of magnitude relative to spontaneous Raman scattering signals.

Femtosecond Stimulated Raman Spectroscopy (FSRS) is a fifth order pump probe technique recently introduced [1,2], which uses SRS as a probe [3–13]. Is has been shown to provide an improved spectral and temporal resolution compared to time resolved-spontaneous Raman. In a typical FSRS experiment, a femtosecond electronically resonant actinic pump pulse triggers vibrational dynamics in an electronically excited state; then, after a variable time delay, the joint action of a picosecond Raman pulse and a femtosecond broadband continuum pulse generates a vibrational coherence which allows to probe the state of the system via the SRS process. The detected signal given by the frequency dispersed transmission of the broadband probe shows both gain and loss Raman features at the red and blue side of the narrowband Raman pulse spectrum [14,15].

In this paper, we address a different scenario in which a femtosecond electronically off-resonant actinic pulse $\mathcal{E}_a$ acts impulsively on the sample to generate ground state rather than an excited state coherences. Depending on the bandwidth of the actinic pulse ($\Delta T_A \simeq 50\,\mathrm{fs}$, which corresponds to $300\,\mathrm{cm}^{-1}$ for a transform limited Gaussian envelope of routinely available ultrafast laser sources), only relatively low frequency modes ($\leq 300\,\mathrm{cm}^{-1}$) of the sample can be excited, leaving it in a vibrational coherent superposition state. Under such circumstances, an ultrashort pulse passing through a medium experiences an upward or downward frequency shift depending on its relative timing after the actinic pulse [16], i.e. a third order Raman process with oscillating Stokes and anti-Stokes intensities is generated. The classical, macroscopic view of this effect is that the molecular vibration, induced by the actinic pulse, generates temporal oscillations in the refractive index. The associated time dependent phase induces a blue or red frequency shift, depending on the derivative sign. These low frequency modes can also couple[17,18], even in the harmonic limit[19], to time delayed Stimulated Raman probing of higher frequency modes, generating a fifth order polarization. It has been already emphasized[18,20] that in molecular liquids the fifth order polarization signals are orders of magnitude smaller than the third order ones and need an attenuation of the overwhelming cascade processes to be detectable. On the other hand, fifth order and cascading processes can be distinguished by their different dependence on chromophore density (linear for the former and quadratic for the latter). Therefore cascading can be suppressed by working at lower densities, which becomes feasible as detection sensitivity is improved. In general, that fifth order processes can be measured in molecular liquids has been demonstrated by R. J. Miller[21,22] and more recently verified by Y. Silberberg (private comunications). Here we extend previous studies of the fifth order polarization within a completely new framework, elucidating the precise microscopic mechanism for the energy transfer between different spectral components of the dispersed FSRS response. The actinic pulse initiates the low frequency vibrational coherences at time $t = 0$, then, after a time delay T, the Raman pulse $\mathcal{E}_p$ and the broadband continuum pulse $\mathcal{E}_s$ stimulate the Raman scattering of a higher frequency vibrational mode. The resulting 2D signal $S(\omega, T)$ depends on the dispersed probe frequency ω and the delay T. Photoinduced structural changes (not included here for sake of simplicity) could cause additional frequency variations. The response of the system is derived by using Closed-Time-Path-Loop (CTPL) diagrams; both the red and the blue side of the spectrum are calculated, providing an unified description of gain and loss processes. Analysis of the two regimes shows that the number of photons of the $\mathcal{E}_s$ field oscillates with T with opposite phase and the same amplitude in the red and in the blue side, therefore the total number of photons is conserved during the process; the total energy of the $\mathcal{E}_s$ field, obtained by the first moment of the transmitted probe frequency profile, shows a damped oscillation. This analysis allows to rationalize third-order experiments as those reported in[16,23].

2 Expressions for FSRS signals

The FSRS process is described by the Hamiltonian

$$H = H_0 + H' + H_f$$

where H_0, H_f and H' represent the free molecule, the radiation field and the effective radiation-matter interaction, respectively. For electronically off-resonance pulses, an excitation to a virtual state is accompanied by an instantaneous de-excitation to a real state, since by the Heisenberg uncertainty principle the system can only spend a very short time on the intermediate state. Therefore, in the rotating wave approximation (RWA), H' reads:

$$H'(t) = \alpha(t) \sum_{i,j} \mathcal{E}_j^\dagger(t)\mathcal{E}_i(t) + h.c. \tag{1}$$

where α is the excited state polarizability

$$\alpha = \sum_{a \neq b} \alpha_{ab} |a\rangle\langle b|$$

and $\mathcal{E} = \sum_j \mathcal{E}_j$ and $\mathcal{E}^\dagger = \sum_j \mathcal{E}_j^\dagger$ are the positive and the negative frequency components of the total electric field operator:

$$E(\mathbf{r}, t) = \sum_j \mathcal{E}_j(t) e^{i\mathbf{k_j}\cdot\mathbf{r}} + \sum_j \mathcal{E}_j^\dagger(t) e^{-i\mathbf{k_j}\cdot\mathbf{r}} \tag{2}$$

For non-overlapping $\mathcal{E}_a(t)$ and $\mathcal{E}_s(t)$ pulses, equation 1 reduces to

$$H'(t) = \alpha(t) \left[\mathcal{E}_s^\dagger(t)\mathcal{E}_p(t) + \mathcal{E}_a^\dagger(t)\mathcal{E}_a(t)\right] + h.c. \tag{3}$$

For non-overlapping ultrashort (off-resonance) $\mathcal{E}_a$ and $\mathcal{E}_s$ pulses, $\mathcal{E}_a$ in the equation is not coupled to the other fields. For non-overlapping ultrashort E_a and E_s pulses this corresponds to the pump-probe technique where the actinic pump generates a photo-excitation that is then detected by the probe. This picture holds also for an off-resonant actinic pulse that generates a ground state coherence.

Stimulated optical signals can be defined as the time derivative of the mean number of photons[24]

$$S = \int_{-\infty}^{+\infty} dt \frac{d}{dt} \left\langle a_i^\dagger(t) a_i(t) \right\rangle = \frac{2}{\hbar} \Im \int_{-\infty}^{+\infty} dt' \left\langle P(t')\mathcal{E}^\dagger(t') \right\rangle = \frac{2}{\hbar} \int_{-\infty}^{\infty} \frac{d\omega'}{2\pi} \Im \left\langle P(\omega')\mathcal{E}^\dagger(\omega') \right\rangle \tag{4}$$

where

$$P(\omega) = \int_{-\infty}^{+\infty} dt e^{i\omega t} P(t) \tag{5}$$

and $P(t) = Tr[V\rho(t)]$ is the nonlinear polarization induced by the interaction and $\langle \ldots \rangle = Tr[\rho(t) \cdot \ldots]$. The frequency-gated signal is then given by

$$S(\omega, T) = \frac{2}{\hbar} \Im \mathcal{E}_s^*(\omega) \int_{-\infty}^{+\infty} e^{i\omega t} \left\langle \mathrm{T} P(t) e^{-\frac{i}{\hbar}\int_{-\infty}^{+\infty} dt'\, H'_-(t')} \right\rangle \tag{6}$$

where H'_- is the Liouville superoperator in the interaction picture and T indicates superoperator time ordering. This expression can be expanded perturbatively in field-matter interactions. In the present application we expand the exponential to fifth order in the fields which yields the 5th order polarization $P^{(5)}$.
The 5th order off-resonant polarization is a convolution of the fields with a three point correlation function of the susceptibility operator. Using the loop diagram representation, it can be easily written directly from the diagram by the application of the rules given in[25]. The diagrams that contribute to the broadband FSRS process are given in Fig. 1. Usually the expressions for the detected signals are derived in terms of nonlinear susceptibilities, using a semiclassical approach, where classical fields interact with a quantum system and they can easily be represented by Double Sided Feynman diagrams or energy level diagrams. While the conventional Double Sided Feynman diagrams description is based on the density matrix (Liouville N^2 dimensional space), the CTPL diagrams one, used in this work, is based on the wavefunction (Hilbert N dimensional space). In the CTPL description the ket (bra) evolution is described by a forward (backward) propagation of the wave function; in the CTPL there is no time-ordering between the left hand side (ket) of the diagram and the right hand side (bra), resulting in fewer contributing terms for a given signal.
We shall work in the frequency domain using a Fourier transform of the field envelopes and define the retarded Green's function

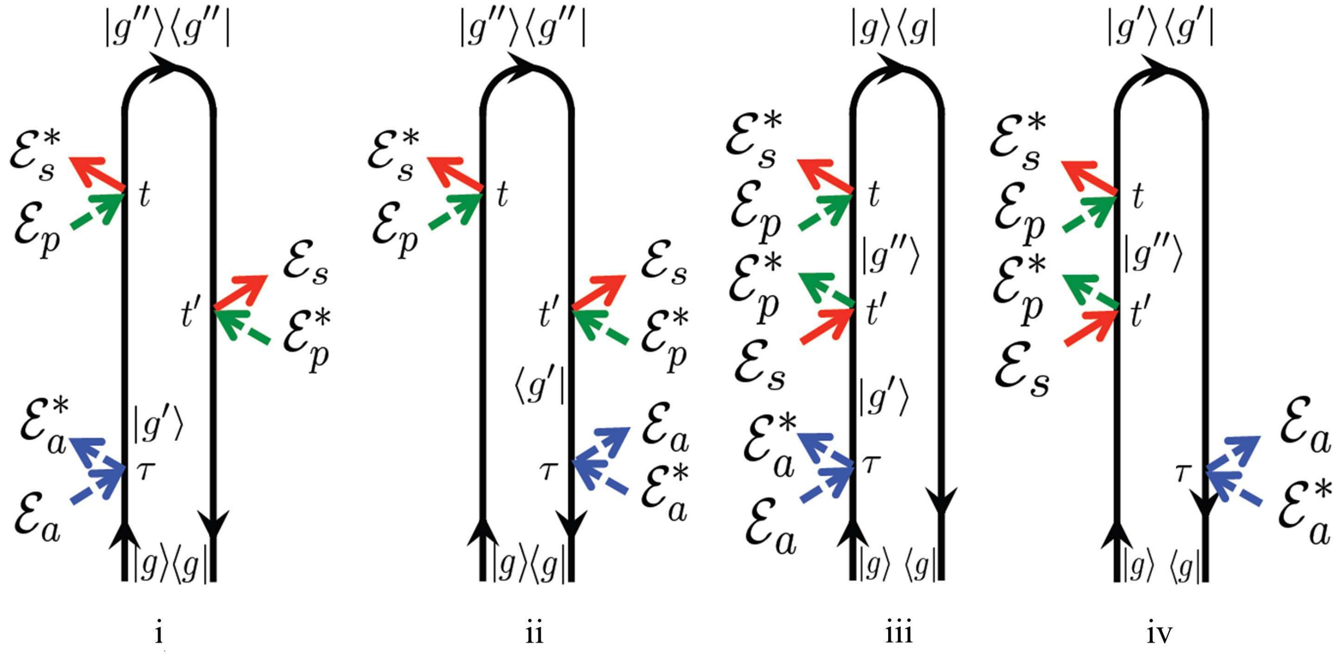

i ii iii iv

Fig. 1: Closed-Time-Path-Loop diagrams for Stimulated Raman with impulsive actinic pump preceding the $\mathcal{E}_s$ field, in off-resonance condition. g refers to the ground state while g' and g'' range over all the vibrational frequencies.

$$G(\omega) = \frac{1}{\hbar(\omega - H_0 + i\eta)} = \frac{1}{\hbar}\sum_\nu \frac{|\nu\rangle\langle\nu|}{\omega - \omega_\nu + i\gamma} \tag{7}$$

and the advanced Green's function

$$G^{\dagger}(\omega) = \frac{1}{\hbar(\omega - H_0 - i\eta)} = \frac{1}{\hbar}\sum_{\nu} \frac{|\nu\rangle\langle\nu|}{\omega - \omega_{\nu} - i\gamma} \tag{8}$$

In both equations 7 and 8 η is a positive infinitesimal that ensures causality and further guarantees the convergence of the Fourier transform. The right hand side of the equations is obtained by an expansion in the molecular eigenstate basis $|\nu\rangle$ and γ is the vibrational dephasing rate.

Reading off the diagrams, we obtain:

$$S(\omega,T) = (-1)^3 P_g\, \Im \int_{-\infty}^{+\infty} \frac{d\Delta_P}{2\pi}\frac{d\omega'_P}{2\pi}\frac{d\Delta}{2\pi}\frac{d\Delta_A}{2\pi}\frac{d\omega'_A}{2\pi}\, 2\pi\, \delta(\Delta_P - \Delta_A - \Delta) e^{-i\Delta_A T}$$
$$\mathcal{E}_p(\omega'_P)\mathcal{E}^*_P(\omega'_P + \Delta_P)\mathcal{E}_s(\omega + \Delta)\mathcal{E}^*_S(\omega)\mathcal{E}_a(\omega'_A + \Delta_A)\mathcal{E}^*_A(\omega'_A)\,(F_i + F_{ii} + F_{iii} + F_{iv}) \tag{9}$$

where $P_i = \left[1 + e^{\beta(E_i - E_g)}\right]^{-1}$, with $\beta = 1/(k_B T)$, represents the thermal occupation of state (i) and all the relevant information about the matter is contained in the following correlation functions of the molecular polarizability which correspond to diagrams $(i) - (iv)$.

$$F_i = \langle \alpha G^{\dagger}(\omega'_P - \omega + \Delta_A)\alpha G(\Delta_A)\alpha \rangle \tag{10}$$
$$F_{ii} = \langle \alpha G^{\dagger}(\omega'_P - \omega)\alpha G^{\dagger}(\Delta - \Delta_P)\alpha \rangle \tag{11}$$
$$F_{iii} = \langle \alpha G(\Delta_A)\alpha G(\omega + \Delta - \omega'_P - \Delta_P + \Delta_A)\alpha \rangle \tag{12}$$
$$F_{iv} = \langle \alpha G^{\dagger}(\Delta - \Delta_P)\alpha G(\omega + \Delta - \omega'_P - \Delta_P)\alpha \rangle \tag{13}$$

The delta function in equation 9 represents the conservation of field energy. The ground state was excluded in eqs. 7 and 8 because that would give a DC background; we are interested in isolating the contributions to the signal due to the excitation of the low frequency modes. The dominant contribution to the signal $S(\omega,T)$ originates from the spectral region in which the denominators of the relevant Green's functions 7 and 8 vanish. The correlation functions 10 and 11 contain an advanced Green's function whose argument contain $\omega'_P - \omega$; diagrams (i) and (ii) then give rise to features on the red side of the Raman pulse. Similarly diagrams (iii) and (iv) lead to signals on the blue side because the retarded Green's function in correlations functions 12 and 13 contains $\omega - \omega'_P$.

The contributions from both sides of the stimulated Raman spectrum have been denoted Stokes and anti-Stokes processes. We next clarify this terminology. The classification of Raman processes as either *Stokes* or *anti-Stokes* originated in spontaneous Raman. The application of this terminology to the stimulated processes has been a source of confusion. According to the common nomenclature, the distinction between Stokes and anti-Stokes processes is based on the temporally last Raman interaction. One speaks of a Stokes process when, due to the last interaction, the molecule passes from a state of lower to higher energy and the emission is red-shifted; conversely in anti-Stokes the last transition is from a state of higher energy to one of lower energy and the emission is blue-shifted. The term Coherent Anti-Stokes Raman Spectroscopy (CARS) comes from this convention. One can alternatively distinguish Stokes and anti-Stokes processes by looking at the overall energy transfer between matter and field, during the entire process with all interactions, not just the last. Stokes processes start from the ground state, $|g\rangle \rightarrow |l/h\rangle$, while anti-Stokes processes start from a vibrational excited states, $|l/h\rangle \rightarrow |g\rangle$. To avoid confusion we simply refer to these signals as red or blue.

The Raman resonance frequencies in a specific diagram depend on the Liouville space pathway. For example in diagram (ii), the pathway $|g\rangle \rightarrow |g'\rangle \rightarrow |g''\rangle$ (with g' and g'' two different vibrational levels of the sample) leads to a response at $\omega_P - \omega''_g$ while the pathway $|g\rangle \rightarrow |g'\rangle \rightarrow |g'\rangle$ leads to a response at $\omega_P - \omega'_g$. This can be seen from the argument of the Green's functions in correlation functions (eq. 10). Hereafter we discuss explicitly the pathways that include both ω'_g and ω''_g; the derivation for the $|g\rangle \rightarrow |g'\rangle \rightarrow |g'\rangle$ pathway is similar.

Diagram (i) leads to a feature at $\omega_P - (\omega''_g - \omega'_g)$. Similarly on the blue side of the Raman pulse, diagram (iii) give rise to a feature at $\omega_P + \omega''_g$ while (iv) gives a response at $\omega_P + (\omega''_g - \omega'_g)$. Therefore there are pathways in Liouville space that do not depend on a single mode but contribute to the signal when different vibrational modes share the same ground state.

In order to simplify equation 9, we use the delta function to carry out the integration over Δ, the bandwidth of the broad $\mathcal{E}_s$ pulse; assuming a monochromatic Raman pulse $\mathcal{E}_p(\omega) = 2\pi E_p \delta(\omega - \omega_P)$ we can reduce eq. 9, without loss of generality, to two integrations:

$$S(\omega,T) = (-1)^3 |E_p|^2 P_g \, \Im \Big[\mathcal{E}_S^*(\omega) \int_{-\infty}^{+\infty} \frac{d\Delta_A}{2\pi} \frac{d\omega'_A}{2\pi} \, e^{-i\Delta_A T} \\ \mathcal{E}_s(\omega+\Delta_A)\mathcal{E}_a(\omega'_A+\Delta_A)\mathcal{E}_A^*(\omega'_A) \left(F_i + F_{ii} + F_{iii} + F_{iv}\right) \Big] \quad (14)$$

which can be expressed as

$$S(\omega,T) = P_g |E_p|^2 \int_{-\infty}^{+\infty} \frac{d\Delta_A}{2\pi} \, S(\omega,T;\Delta_A) \quad (15)$$

with

$$S(\omega,T;\Delta_A) = (-1) \, \Im \Big[\mathcal{E}_S^*(\omega) \int_{-\infty}^{+\infty} \frac{d\omega'_A}{2\pi} \, e^{-i\Delta_A T} \\ \mathcal{E}_s(\omega+\Delta_A)\mathcal{E}_a(\omega'_A+\Delta_A)\mathcal{E}_A^*(\omega'_A) \left(F_i + F_{ii} + F_{iii} + F_{iv}\right) \Big] \quad (16)$$

The Δ_A dispersed signal of eq. 16 is not an observable quantity since it contains more information than the experimental signal $S(\omega,T)$ [26].

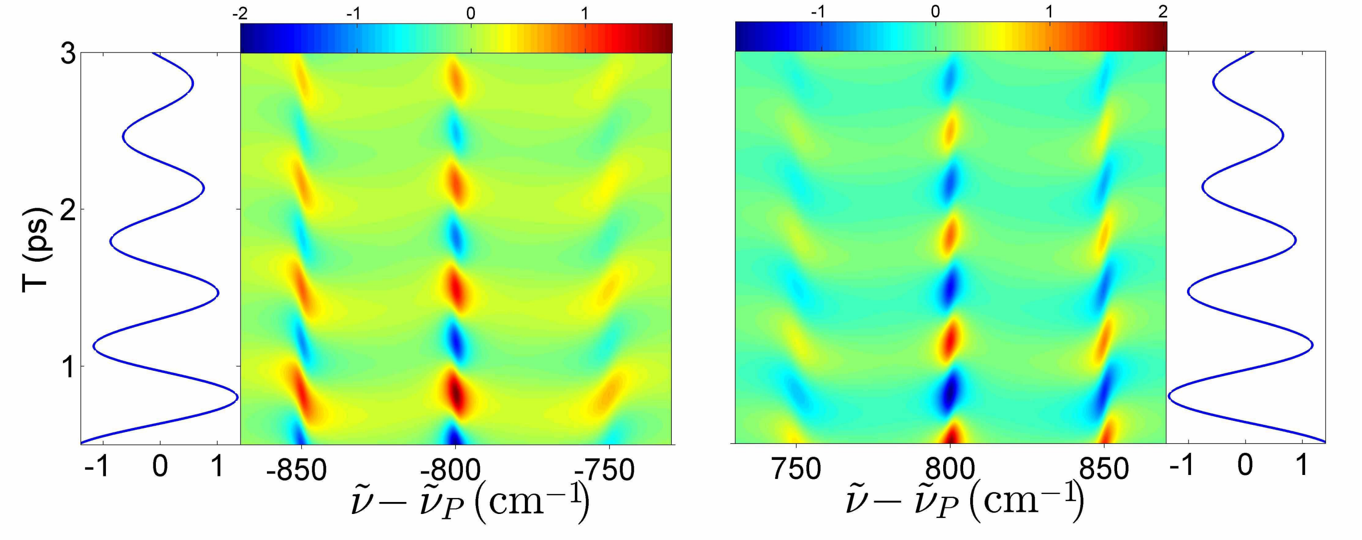

Fig. 2: Two dimensional plot of $S(\omega,T)$, eq. 14, for Diagrams (i) and (ii) (on the left) and Diagrams (iii) and (iv) (on the right), for a system with one low ($\tilde{\nu}_l = \omega_l/c = 50\,\mathrm{cm}^{-1}$) and one high frequency mode ($\tilde{\nu}_h = 800\,\mathrm{cm}^{-1}$); the vibrational dephasing time is $\gamma_l^{-1} = \gamma_h^{-1} = 2.3\,\mathrm{ps}$.. In side panels we show the integrals of the signal over the detected frequency that give the number of photons in the red and in the blue side of the spectrum.

3 Signal simulations

We consider a two mode harmonic molecular system, with one low frequency mode ($\tilde{\nu}_l = \omega_l/2\pi c = 50\,\mathrm{cm}^{-1}$) and one high frequency mode ($\tilde{\nu}_h = 800\,\mathrm{cm}^{-1}$). Three vibrational states contribute to the sum over states expression (eq. 14): the high frequency excited state at ω_h, the low frequency excited state at ω_l and a state at $\omega_h + \omega_l$ in which both vibrational modes are excited. Accounting for all possible Liouville pathways, both diagram (i) and (ii) contribute to a feature at $\omega_P - \omega_h$; the former generates also a side peak shifted to the red of the main feature at $\omega_P - (\omega_h - \omega_l)$ while the latter gives a side peak shifted to the blue at $\omega_P - (\omega_h + \omega_l)$. Similarly, diagrams (iii) and (iv) give rise to a central feature at $\omega_P + \omega_h$ and two side bands. In the present harmonic model the two side bands have the same phase and exhibit a similar behavior, as shown in Fig. 2 where we display the signal $S(\omega, T)$ for different time delays T. Both the actinic pulse $\mathcal{E}_a$ and the broadband pulse $\mathcal{E}_s$ have a Gaussian envelope with a FWHM of 20 fs and 10 fs, respectively. We emphasize that $S(\omega, T)$, which is proportional to the fifth order polarization $P^{(5)}$, appears as a correction to the stronger $P^{(3)}$ contribution in the total FSRS signal. The actinic-off signal consists of a sharp positive peak centered in $\omega_P - \omega_h$ and a sharp negative peak centered in $\omega_P + \omega_h$. When the actinic pulse is switched on, additional features compare at $\omega_P \pm (\omega_h \pm \omega_l)$. As predicted in[19], and quantitatively highlighted in Fig. S3, the inclusion of anharmonicity does not substantially changes the above scenario, except for a possible π phase shift between relative sidebands associated to the same low frequency mode ω_l. The main as well as the side bands evolve from an absorptive peak to a dispersive shape depending on the delay T. In the side panels of Fig. 2, we show the behavior in time of the number of photons in the red and the blue side of the spectrum, obtained as the integral of $S(\omega, T)$ over the detected frequency ω:

$$N_{red}(T) = \int_{-\infty}^{\omega_P} d\omega S(\omega, T) \tag{17}$$

$$N_{blue}(T) = \int_{\omega_P}^{\infty} d\omega S(\omega, T) \tag{18}$$

For each time delay the signal $S(\omega, T)$ is a sum of dispersive and gain/loss absorptive contributions. Only the latter contribute to the integrated signal of eqs. 17 and 18 since the dispersive ones cancel out, the gain/loss components of the side bands contributes coherently. Both $N_{red}(T)$ and $N_{blue}(T)$ exhibit damped oscillations in T with the same amplitude and period but opposite phase. This numerical result can be derived by making some simplifying assumptions. We focus on the response at

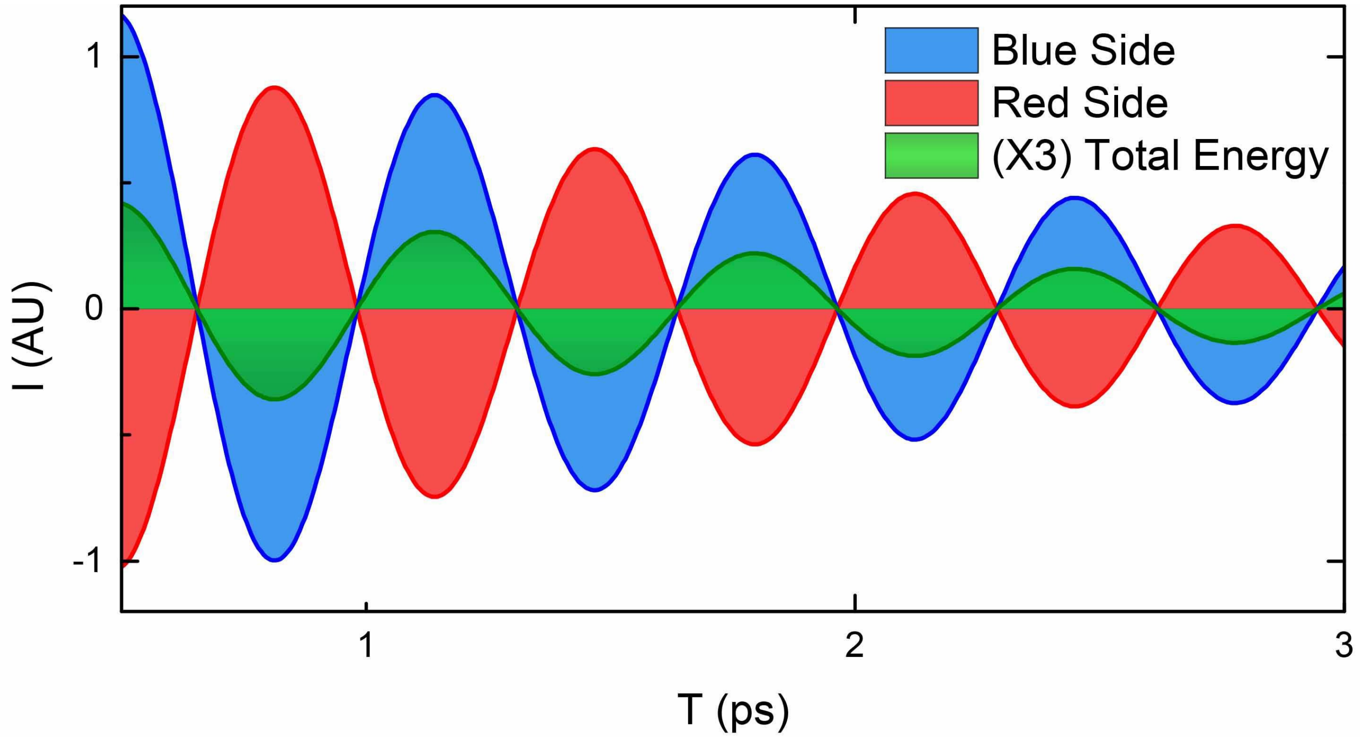

Fig. 3: Total Energy Balance; the red line indicates the energy oscillation of the signal in the red side of the spectrum, obtained multiplying the number of photons of Fig. 2 by $\hbar\omega$, while the blue line indicates the energy oscillation in the blue side of the spectrum. The green line shows the total energy oscillation (after a 3-fold expansion). While the total number of photons is conserved in the process, this symmetry is slightly broken if we consider the total energy.

$\pm(\omega_P - \omega_h)$ generated by diagrams (ii) and (iv). The other contributions can be obtained similarly. For impulsive $\mathcal{E}_s$ and $\mathcal{E}_a$ pulses and a monochromatic $\mathcal{E}_p$ pulse we have

$$N_{red}(T) = -V_\Omega |E_p|^2 |E_s|^2 P_g \,\Im\left[\int_{-\infty}^{+\infty} \frac{d\omega}{2\pi}\frac{d\Delta_A}{2\pi}\frac{e^{-i\Delta_A T}}{[(\omega_P - \omega - \omega_h - i\gamma_h)\,(-\Delta_A - \omega_l - i\gamma_l)]}\right] \tag{19}$$

for the red side, and

$$N_{blue}(T) = -V_\Omega |E_p|^2 |E_s|^2 P_g \,\Im\left[\int_{-\infty}^{+\infty} \frac{d\omega}{2\pi}\frac{d\Delta_A}{2\pi}\frac{e^{-i\Delta_A T}}{[(\omega - \omega_P - \omega_h + i\gamma_h)\,(\Delta_A - \omega_l + i\gamma_l)]}\right] \tag{20}$$

for the blue side. V_Ω indicates the quantization volume of the actinic frequencies. Contour integration over Δ_A is performed

$$N_{red}(T) \propto -\Im\left[\int_{-\infty}^{+\infty} \frac{d\omega}{2\pi}\frac{i\gamma e^{-i\omega_l T - \gamma_l T}}{(\omega_P - \omega - \omega_h - i\gamma_h)}\right] \tag{21}$$

The denominator in eq.21 gives a Lorentzian profile

$$\frac{1}{\omega_P - \omega - \omega_h - i\gamma_h} = (\omega_P - \omega - \omega_h + i\gamma_h)\, L(\omega_P - \omega - \omega_h)$$

which reduces to $i\gamma_h\delta(\omega_P - \omega - \omega_h)$ for small γ_h. This gives

$$N_{red}(T) \propto e^{-\gamma_l T}\sin(\omega_l T) \tag{22}$$

and

$$N_{blue}(T) \propto -e^{-\gamma_l T}\sin(\omega_l T) \tag{23}$$

The total number of photons in the $\mathcal{E}_s$ field is conserved. While the frequency dispersed signal is dominated by the high frequency mode, the information on ω_h is completely lost in a detection of the total field intensity (for example performed with a photodiode); the oscillation period ($T_N = \frac{2\pi}{\omega_l}$) and the damping factor (γ_l) are determined by the low frequency mode.
Fig. 3 shows the total transmitted energy of the signal, obtained multiplying the number of photons 18 by $\hbar\omega$, for the red and blue side of the spectrum separately and the total energy oscillation (green line). While the number of photons is conserved in the process, the total pulse energy $I(T) = \int_{-\infty}^{\infty} d\omega S(\omega, T)\omega$ does change.

The role of the actinic pulse is better demonstrated by considering a system with more than one low frequency vibrational mode. In Fig. 4 we use the Δ_A dispersed signal (eq. 16) to study the response of a sample with four low frequency modes ($50\,\mathrm{cm}^{-1}$, $80\,\mathrm{cm}^{-1}$, $110\,\mathrm{cm}^{-1}$ and $173\,\mathrm{cm}^{-1}$) and one high frequency mode ($800\,\mathrm{cm}^{-1}$). For simplicity we consider explicitly levels ω_g, ω_l and ω_h in which only a single mode is excited.
$S(\omega, T = 500\,\mathrm{fs}; \Delta_A)$ is displayed for various bandwidths of the actinic pump (20 fs 80 fs and 150 fs of time duration), only the shorter actinic pump pulse is able to excite all the low frequency modes, while the longer pulse can only excite a narrower band of frequencies. The only frequencies of the actinic pulse involved in the process are those involved in the coherence generation with the low frequency mode, belonging to a small region around the resonances. Since the generated coherence is detected at $\omega = \omega_P - (\omega_h - \omega_l)$ (difference between the high and the low frequency mode), reducing the actinic bandwidth truncates the contributions of lower wavenumber frequency far from $\omega = \omega_P - \omega_h$.

Figure 5 depicts the response of this multi-mode system for an 80 fs actinic pump, showing the time delay dependence of the frequency dispersed spectra and of the frequency integrated signal. The behavior of $N(T)$ is more complex than for a single low frequency mode, since the signal results from the sum of four damped sinusoids, with different amplitudes, depending on the bandwidth of the actinic pump pulse. The contribution from the low modes involved is directly extracted disentangling the four components by the Fourier transform over T of $S(\omega, T)$

$$S(\omega, \Omega) = \int_{-\infty}^{\infty} e^{-i\Omega T} S(\omega, T) \tag{24}$$

which is reproduced in the right panel of Fig. 5. The number of photons $N(T)_{red}$ in the red side and $N(T)_{blue}$ in the blue side varies with opposite phase, and the overall number of photons is still conserved.

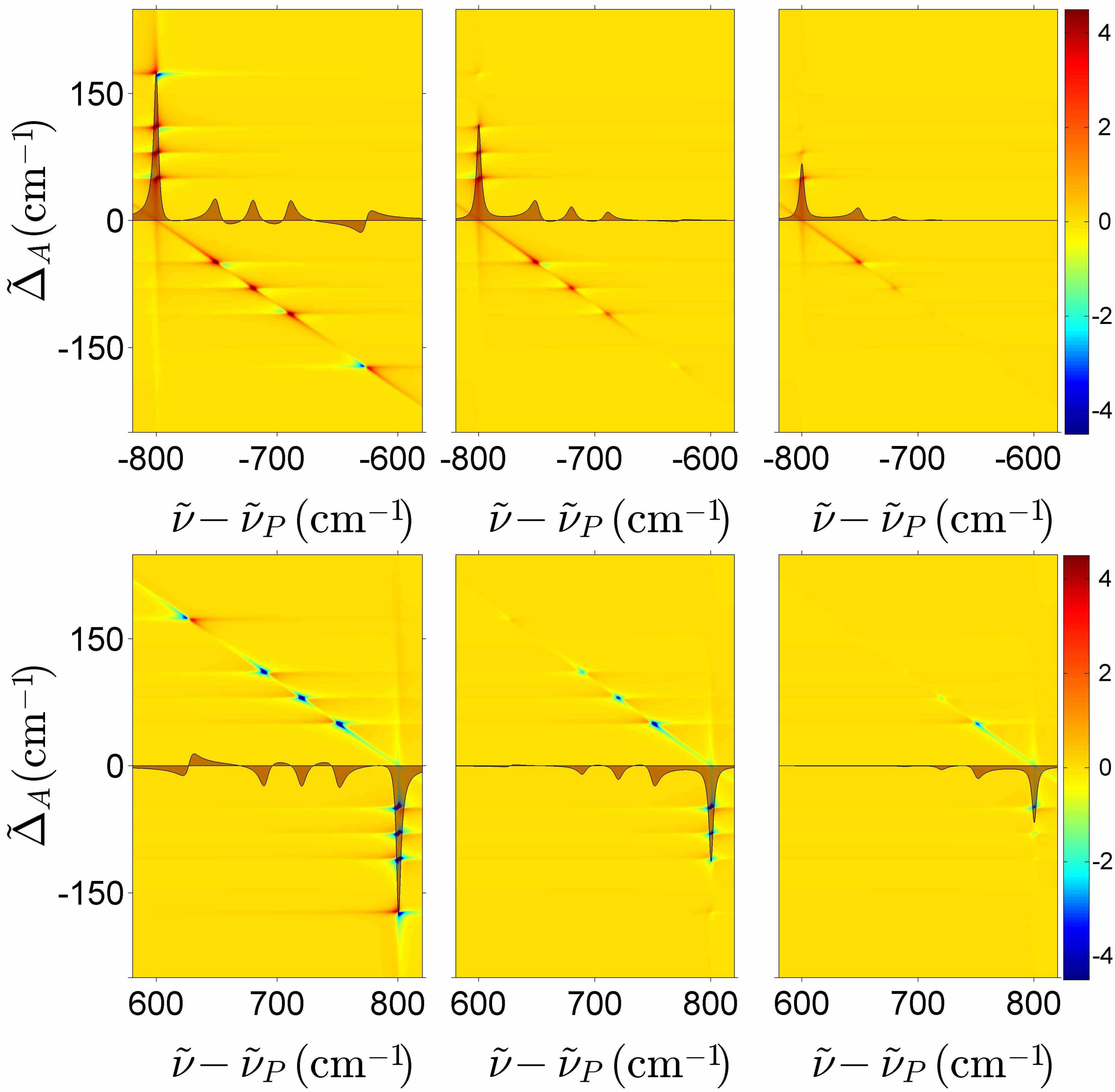

Fig. 4: Δ_A dispersed signal (eq. 16) and corresponding integrated signal for diagrams (i) and (ii) (top panel) and (iii) and (iv) (bottom panel) for a system with four low frequency modes ($50\,\mathrm{cm}^{-1}$, $80\,\mathrm{cm}^{-1}$, $110\,\mathrm{cm}^{-1}$ and $173\,\mathrm{cm}^{-1}$) and one high frequency mode ($800\,\mathrm{cm}^{-1}$), calculated at 500 fs of time delay T. The 2D plot of $S(\tilde{\nu}, T = 500\,\mathrm{fs}; \Delta_A)$ are reported varying the bandwidth of the actinic pump (20 fs, 80 fs and 150 fs of time duration, from the left to the right), showing that a narrower actinic pump pulse is not able to excite all the low frequency modes. The shaded black area reproduces the integral $S(\tilde{\nu}, T = 500\,\mathrm{fs})$ signal over Δ_A, showing a much more intense contribution at $\tilde{\nu} - \tilde{\nu}_P = \pm\tilde{\nu}_H$.

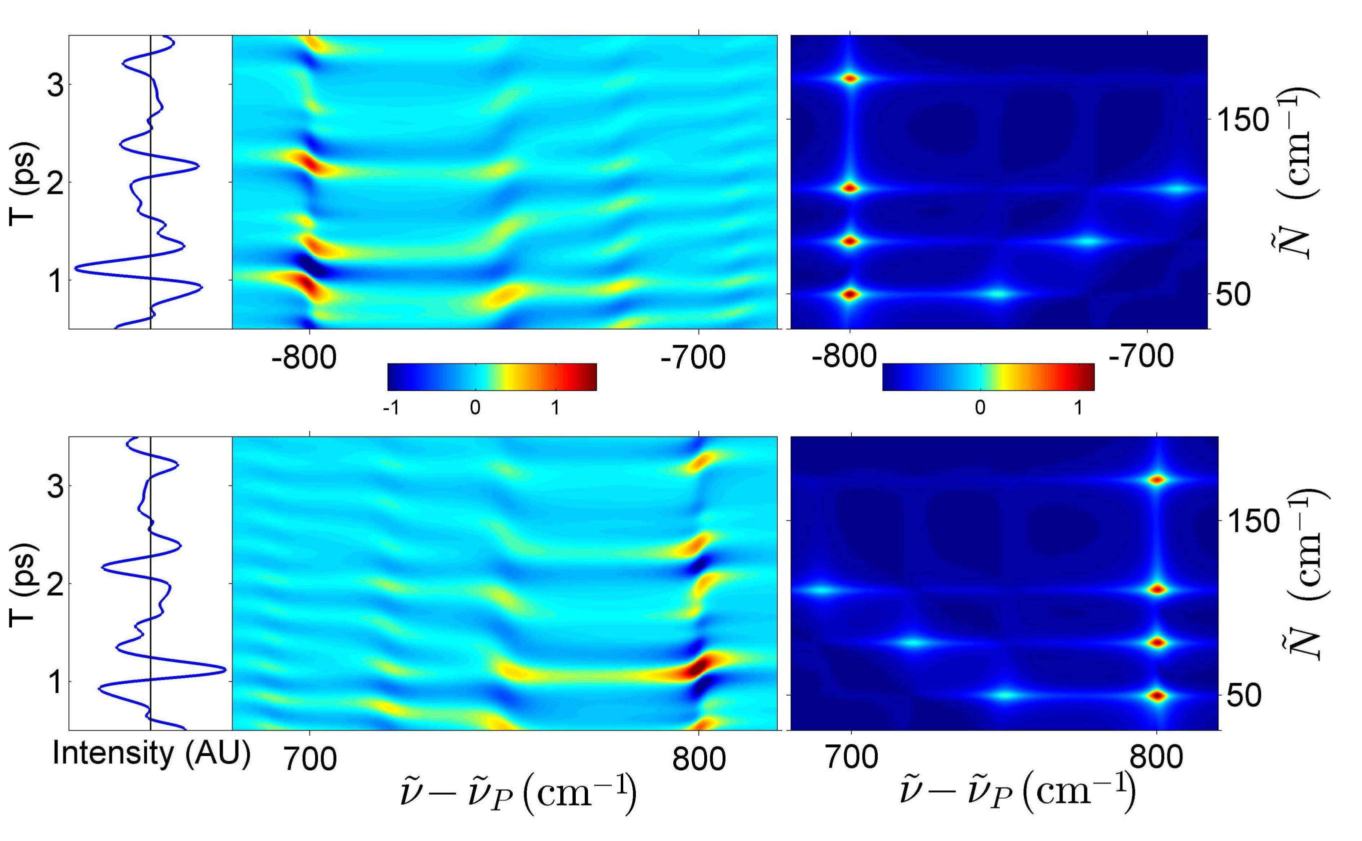

Fig. 5: Central Panel: Time delay dependent 2D signal $S(\tilde{\nu}, T)$ of diagrams (i) and (ii) (top) and of diagrams (iii) and (iv) (bottom); the response is calculated for a system with four low frequency modes ($50\,\mathrm{cm}^{-1}$, $80\,\mathrm{cm}^{-1}$, $110\,\mathrm{cm}^{-1}$ and $173\,\mathrm{cm}^{-1}$) and one high frequency mode ($800\,\mathrm{cm}^{-1}$) using an 80 fs actinic pump. The number of photons $N_{red/blue}(T)$ is reproduced in the left panel, while in the right one the contributions from all the low frequency modes are disentangled by the Fourier transform $S(\tilde{\nu}, \tilde{N})$.

4 Conclusions

In this paper we have employed a microscopic diagrammatic approach to the Broadband Stimulated Raman Spectroscopy with an impulsive off-resonant actinic pump. Expressions for both the red and the blue side of the spectrum are derived. The coherences created by the impulsive pump cause modifications of the resulting Raman signal as a function of the time delay between the pump and probe pulses, that varies from gain to loss features. The interplay of these features is responsible for a redistribution of photons between the two sides of the spectrum that conserves the total number of photons but leads to an energy flow between fields and matter.

In particular, we have considered three detection modes for fifth-order stimulated Raman measurements that include an actinic initial excitation: the partially integrated red $N_{red}(T)$ or blue $N_{blue}(T)$ (Fig. 2), the frequency integrated 1D signal $I(T)$ (Fig. 3) and the fully dispersed $S(\omega, T)$ (Fig. 2). The first two are 1D and the last is a 2D technique. The integrated signal $I(T)$ probes the total energy exchange between the molecule and the field which reveals Raman resonances. This is also seen by the shift in the blue/red detection. The frequency resolved spectrum carries more information and can show dispersive features which do not contribute to the molecule/field energy exchange[27]. Ideguchi *et al.*[16,23] had employed the partially integrated detection for a third order measurement of intensity fluctuations and obtained a similar oscillatory behavior as in our eqs. 22 and 23 and Fig. 3.

In a third order experiment the energy flow manifests itself as time domain intensity fluctuations, which can be interpreted as an apparent red and blue shift of the probe pulse[28]. While information on the low frequency vibrational modes of the medium can be retrieved by a Fourier transform, the temporal evolution of the spectrally resolved optical probe is not accessible. The integrated signal directly obtained in[16] can be easily recast from the dispersed signal as we have shown in Fig. 2. In addition, the time resolution brought about the fifth order process enables the collection of snapshots of the energy transfer pathway, while the frequency dispersed detection allows dissecting the time dependence of the contribution corresponding to a single spectral component. Although this does not provide additional information from the material perspective, it reveals the mechanism underlying the energy redistribution pathway. Specifically, as seen in Fig. 2 the low frequency coherence does not generate a spectral shift but rather a modulation of the first momentum of the broadband probe spectrum.

5 Acknowledgements

S.M. is grateful for the hospitality and support while at the Universitá di Roma “Sapienza” as a Visiting Professor and gratefully acknowledges the support of the National Science Foundation through Grant No. CHE- 1361516, the Chemical Sciences, Geosciences and Biosciences Division, Office of Basic Energy Sciences, Office of Science, U.S. Department of Energy, and a National Institute of Health Grant No. GM-59230.

Supplementary Material

The detected signals can be directly derived from the CTPL diagrams by the use of the following rules:

1. Time runs clockwise along the loop from the bottom left to the bottom right.
2. The interactions within each branch are time ordered, but interactions on different branches are not. Each loop can be further decomposed into several fully-time-ordered diagrams (double-sided Feynman diagrams).
3. A field mode is represented by an arrow.
4. The loop contains a series of interactions, depicted as intersection between the loop and the arrows. Interactions are separed by periods of free evolutions s_i, forwards in real time on the left branch and backwards on the right branch.
5. Arrows pointing to the right represent interaction with the field annihilation operator $\mathcal{E}_j(\omega)$, while arrows pointing to the left represent interaction with the field creation operator $\mathcal{E}_j^\dagger(\omega)$. The interactions are with a couple of arrows $\mathcal{E}_i\mathcal{E}_j^\dagger$ and are accompanied by the polarizability α.
6. For each period of free evolution on the left branch we write a retarded Green's function $G(\sum_j \omega_j)$, where the sum goes over all earlier interactions along the loop, i.e. the frequency arguments of the various propagators are cumulative; additionally, the ground state frequency ω_g is added to all arguments of the propagators. Similarly for each period of free evolution on the right branch we write an advanced Green's function $G^\dagger(\sum_j \omega_j)$.
7. The interaction at the observation time t is fixed to be with the detected mode and is always the last. It is chosen to be on the left branch of the loop.
8. The overall sign of the correlation function is given by $(-1)^{N_{int}}$, where N_{int} is the number of interactions along the loop, i.e. the number of intersections between the loop and the arrows.
9. Signal expression contains a delta function $2\pi\,\delta(\sum_{j=1}^{n+1}\omega_j)$, accounting for energy conservation.

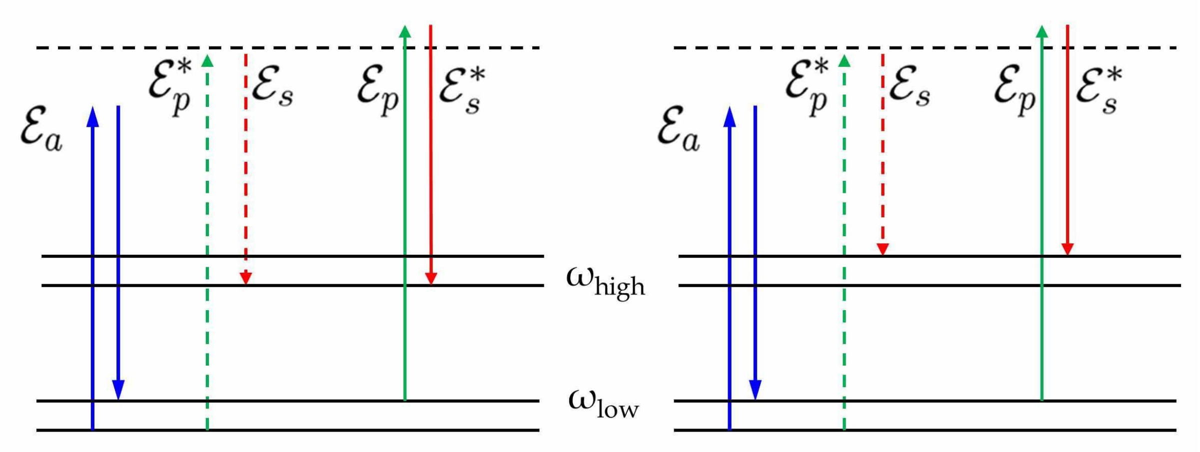

Fig. S1: Energy-level diagrams corresponding to term *i* of Fig. 1.

Loop diagrams of Fig. 1 can be recasted in term of Double-Sided Feynman or energy level diagrams. For example in Fig. S1 we present the energy level diagrams which correspond to the term i of Fig. 1, producing contributions at $\omega_P - (\omega_h - \omega_l)$ and $\omega_P - \omega_h$.

In Fig. S3 we provide a quantitative comparison with some previous theoretical treatments of Lee[19], where the fifth-order response of a $\mathrm{CDCl_3}$ molecule is calculated; here we verify that our results can be simply applied to the systems studied by Lee and that the general harmonic potential used in our paper guarantees phase conservation for the sidebands associated to the same low frequency mode, while the anharmonic potential can produce a 180 degrees shift of the relative phases.

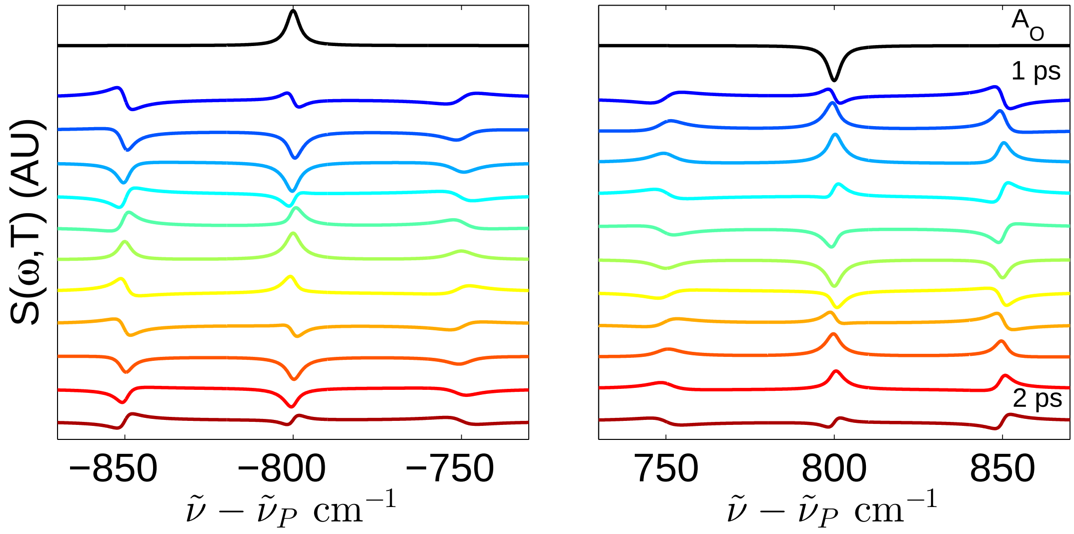

Fig. S2: Slices of Fig. 2 signal at different time delays, from 1 ps to 2 ps in steps of 100 fs, are reproduced and compared to the third order (normalized) response of the system without the actinic impulsive excitation, reproduced by the black line.

References

1 M. Yoshizawa, Y. Hattori and T. Kobayashi, *Phys. Rev. B*, 1994, **49**, 13259–13262.
2 D. W. McCamant, P. Kukura, S. Yoon and R. A. Mathies, *Rev. Sci. Instrum.*, 2004, **75**, 4971.
3 P. Kukura, D. W. McCamant, S. Yoon, D. B. Wandschneider and R. A. Mathies, *Science*, 2005, **310**, 1006–1009.
4 S. Laimgruber, H. Schachenmayr, B. Schmidt, W. Zinth and P. Gilch, *Appl. Phys. B*, 2006, **85**, 557–564.
5 C. Fang, R. R. Frontiera, R. Tran and R. A. Mathies, *Nature*, 2009, **462**, 200–204.
6 S. A. Kovalenko, A. L. Dobryakov and N. P. Ernsting, *Rev. Sci. Instrum.*, 2011, **82**, 063102.
7 A. L. Dobryakov, I. Ioffe, A. A. Granovsky, N. P. Ernsting and S. A. Kovalenko, *J. Chem. Phys.*, 2012, **137**, 244505.
8 E. Pontecorvo, S. Kapetanaki, M. Badioli, D. Brida, M. Marangoni, G. Cerullo and T. Scopigno, *Opt. Express*, 2011, **19**, 1107.
9 E. Pontecorvo, C. Ferrante, C. G. Elles and T. Scopigno, *Opt. Express*, 2013, **21**, 6866–6872.
10 E. Pontecorvo, C. Ferrante, C. G. Elles and T. Scopigno, *J. Phys. Chem. B*, 2014, **118**, 6915–6921.
11 H. Kuramochi, S. Takeuchi and T. Tahara, *J. Phys. Chem. Lett.*, 2012, **3**, 2025–2029.
12 F. Provencher, N. Bérubé, A. W. Parker, G. M. Greetham, M. Towrie, C. Hellmann, M. Côté, N. Stingelin, C. Silva and S. C. Hayes, *Nat Comms*, 2014, **5**, 4288.
13 M. Kloz, R. van Grondelle and J. T. Kennis, *Phys. Chem. Chem. Phys.*, 2011, **13**, 18123.
14 B. Mallick, A. Lakhsmanna and S. Umapathy, *Journal of Raman Spectroscopy*, 2011, **42**, 1883–1890.

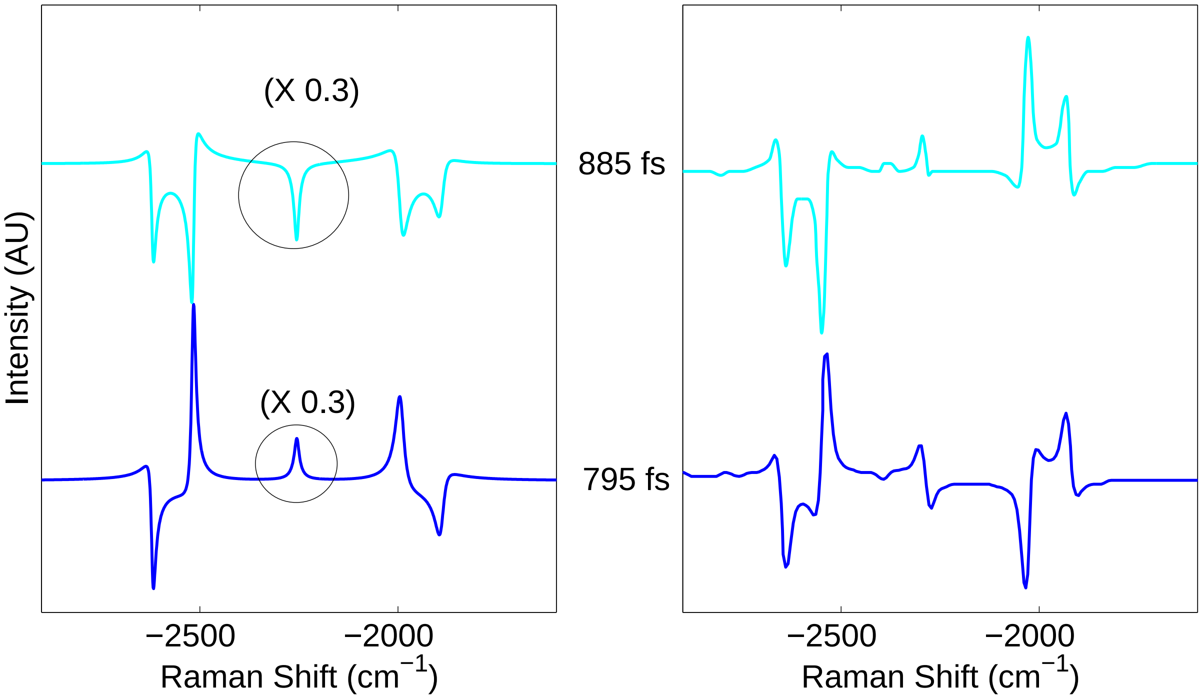

Fig. S3: Comparison between our results (reduced to the red side of the spectrum on the left panel) and the ones obtained in[19] by Lee et al. (reproduced on the right panel for the red side of the spectrum), where the fifth-order response of a $\mathrm{CDCl_3}$ molecule with an high frequency mode at $2255\,\mathrm{cm}^{-1}$ and two low frequency modes at respectively $262\,\mathrm{cm}^{-1}$ and $365\,\mathrm{cm}^{-1}$. The work of Lee considers an anharmonic potential, which produces a 180 degrees relative phase modification of the sidebands, while the harmonic potential used in our work guarantees phase conservation for sidebands associated to the same low frequency modes.

15 U. Harbola, S. Umapathy and S. Mukamel, *Phys. Rev. A*, 2013, **88**, 011801.
16 T. Ideguchi, S. Holzner, M. Yan, G. Guelachvili, T. W. Hänsch and N. Picqué, *arXiv:1403.3814*, 2014.
17 P. Kukura, R. Frontiera and R. A. Mathies, *Phys. Rev. Lett.*, 2006, **96**, 238303.
18 R. D. Mehlenbacher, B. Lyons, K. C. Wilson, Y. Du and D. W. McCamant, *J. Chem. Phys.*, 2009, **131**, 244512.
19 Z. Sun, B. Fu, D. H. Zhang and S.-Y. Lee, *J. Chem. Phys.*, 2009, **130**, 044312.
20 B. Dunlap, K. C. Wilson and D. W. McCamant, *J. Phys. Chem. A*, 2013, **117**, 6205–6216.
21 K. J. Kubarych, C. J. Milne and R. J. D. Miller, *International Reviews in Physical Chemistry*, 2003, **22**, 497–532.
22 C. J. Milne, Y. L. Li, T. l. C. Jansen, L. Huang and R. J. D. Miller, *J. Phys. Chem. B*, 2006, **110**, 19867–19876.
23 T. Ideguchi, S. Holzner, B. Bernhardt, G. Guelachvili, N. Picqué and T. W. Hänsch, *Nature*, 2013, **502**, 355–358.
24 K. E. Dorfman, B. P. Fingerhut and S. Mukamel, *J. Chem. Phys.*, 2013, **139**, 124113.
25 S. Rahav and S. Mukamel, *Advances in Atomic, Molecular, and Optical Physics*, 2010, vol. 59.
26 B. P. Fingerhut, K. E. Dorfman and S. Mukamel, *J. Chem. Theory Comput.*, 2014, **10**, 1172–1188.
27 S. Rahav and S. Mukamel, *Proceedings of the National Academy of Sciences*, 2010, **107**, 4825–4829.
28 Y. Silberberg, *Nature*, 2013, **502**, 307–308.